Impact damage of composite laminates with high-speed waterjet

Hou, Naidan; Zhao, Renxi; Li, Jian; Wang, Xuan; Li, Xi; Cui, Hao; Li, Yulong

DOI
10.1016/j.ijimpeng.2022.104276

Publication date
2022

Document Version
Final published version

Published in
International Journal of Impact Engineering

International Journal of Impact Engineering 167 (2022) 104276

Contents lists available at ScienceDirect

International Journal of Impact Engineering

journal homepage: www.elsevier.com/locate/ijimpeng

Impact damage of composite laminates with high-speed waterjet

Naidan Hou [a,b,c], Renxi Zhao [a,b,c], Jian Li [a,b,c], Xuan Wang [a,b,c], Xi Li [d], Hao Cui [e,f,*], Yulong Li [b,c,e,f,*]

[a] School of Aeronautics, Northwestern Polytechnical University, Xi'an, China
[b] Joint International Research Laboratory of Impact Dynamics and Engineering Application, Xi'an, China
[c] Shaanxi Key Laboratory of Impact Dynamics and Engineering Application, Xi'an, China
[d] Structural Integrity & Composites Group, Faculty of Aerospace Engineering, Delft University of Technology, Kluyverweg 1, 2629HS Netherlands
[e] School of Civil Aviation, Northwestern Polytechnical University, Suzhou, China
[f] NPU Yangzi River Delta Research Institute, Suzhou, Jiangsu, China

ARTICLE INFO

Keywords:
Liquid impact
CFRP
Water-hammer pressure
Finite element analysis
Damage mechanics

ABSTRACT

Rain erosion may cause substantial damage to aircrafts during supersonic flight. Such event is investigated here via high-speed waterjet impact on composite laminates. An experimental setup is developed to produce waterjets with the speed up to 700m/s and a finite element model of the waterjet-composite impact event is established. The consistency of experiment and simulation results validates the adopted numerical methods. The distribution of the water-hammer pressure is non-uniform and the maximum pressure occurs near the contact periphery when the water is about to eject laterally. After a high-speed (300~560m/s) waterjet impacts a composite laminate, the impacted surface depression is observed, and the typical surface damage presents a central region with no visible surface damage surrounded by a faded "failure ring" with resin removal, matrix cracking and minor fiber fracture. Delamination occurs at the interfaces of adjacent layers with unequal dimensions and longitudinal matrix cracking appears on the back surface. Both the velocity and the diameter of waterjets are crucial factors on CFRP damage extents. Water-hammer pressure, the stagnation pressure and propagation of stress waves are failure mechanisms for most matrix damage in CFRP impacted by waterjets.

1. Introduction

Rain erosion on aircrafts during flight has been reported for decades [1–4]. Such an encounter may arise when an aircraft traverses a cloud formation or when it becomes exposed to precipitation. The subject of liquid droplet impingement (LDI) on solid materials was extensively investigated dating back to the early 1950s, with the main focus of the isotropic materials including metals [5], polymers [6], ceramics [7] and rocks [8,9]. Few investigations were conducted on rain impact resistance of anisotropic materials such as carbon fiber reinforced polymers (CFRP), which is one of the most widely-used materials in aircraft structures. Hancox [10] studied the erosion behavior of unidirectional CFRP by repeated impact with liquid jets at velocities of up to 90 m/s, with individual fiber cracking and pits observed on the impacted surface. Gorham and Field [11] investigated the impact properties of CFRP by waterjets with higher velocities (up to 700m/s), in which the basic damage modes were presented as the undamaged center surrounded by a failure ring on the impacted surface.

Since liquid impact event features small spatial and temporal scales, numerical simulation thus emerges as a more convenient and powerful tool to evaluate the stress, strain, and deformation fields for liquid-solid impact analysis, which would be costly and difficult to reproduce experimentally or theoretically. The majority of numerical research focused mainly on the hydrodynamics of the liquid, rather than the target material response to it [12–14]. Therefore, the solid material was frequently simplified to rigid or elastic-plastic model. Among those studies in which the deformation and failure of the solid were considered, isotropic materials especially polymethylmethacrylate (PMMA) were extensively investigated [15–17] while none of the studies simulates the damage initiation and evolution of a CFRP laminate during waterjet impact to authors' knowledge. Some fundamental principles of liquid-CFRP impact also remain unclear and are summarized as follows. Firstly, it is well understood that symmetric pressure distribution and damage patterns are generated in isotropic materials, while how the stress distribution and damage patterns are presented on the anisotropic materials like CFRP laminates subjected to liquid impact is still lack of

* Corresponding author.
E-mail addresses: hao.cui@nwpu.edu.cn (H. Cui), liyulong@nwpu.edu.cn (Y. Li).

https://doi.org/10.1016/j.ijimpeng.2022.104276
Received 20 May 2021; Received in revised form 17 April 2022; Accepted 11 May 2022
Available online 15 May 2022

comprehension. Secondly, Hsu et al. [17] reported that their simulation results of hydraulic impact pressures generated on PMMA substrate were in good agreement with one-dimensional (1-D) water-hammer pressure equation presented by Cook [18]. When it comes to a CFRP laminate, whether the 1-D empirical formulas are still applicable for the estimation of water-hammer pressure remains to be explored. Additionally, though some typical failure characteristics of CFRP under waterjet impact were observed in previous studies, their underlying mechanisms are still ambiguous and lack of concrete evidence.

The goal of the present study is to reveal the dynamic response and failure mechanism of CFRP laminates subjected to liquid impact by the means of combining experimental research with numerical simulation. In Section 2, basic theories of liquid-solid impingement and common approximations of water-hammer pressure are overviewed. A typical waterjet generating apparatus is introduced in Section 3 and experiments of single waterjet impact were carried out on CFRP specimens. Section 4 developed a finite element model in which the damage initiation and evolution of each ply of CFRP laminates can be displayed during waterjet impact. Simulation results of the mechanical response as well as failure patterns of CFRP laminates impacted by waterjets are presented and compared with experiments in Section 5. Failure mechanism of each damage mode is analyzed and the effects of the velocity and diameter of the waterjets are assessed by parameter studies. Finally, some conclusions are highlighted in Section 6. This paper strikes to gain an insight into the fundamental mechanical behavior of CFRP laminates encountering high-speed waterjet impact, and lay the groundwork of the rain impact resistance design of supersonic aircrafts.

2. Liquid-solid impingement theory

Liquid-solid impact process involves two stages: liquid compression and lateral jetting. At the initial contact when the liquid impacts on the solid, the contact boundary moves faster than the shock wave inside the liquid and hence a series of wavelets are hindered to form a shock envelope, shown in Fig. 1(a). The liquid within the envelope is compressed and induces a transient high pressure known as "water hammer pressure". Though there are plenty of empirical formulas aiming to determine the analytic value of the water-hammer pressure, a consensus is still not reached. The concept of the water-hammer pressure is initially introduced by Cook [18] and this impulsive pressure can be estimated by,

$$P_{\mathrm{wh}} = \rho_0 C_0 V \tag{1}$$

in which ρ_0 is the liquid density, C_0 is sound speed of the liquid and V is liquid impact velocity. Heymann [19] argued that this approximation is not valid in higher speed regimes since the shock wave speed does not equal to the sonic speed taking into account the compressibility of the liquid. Hence the impact pressure is modified by Heymann's equation,

$$P_{\mathrm{H}} = \rho_0 C_0 V(1 + kM_0) \tag{2}$$

where k denotes a material constant related to liquid compressibility and is close to 2 for water in the velocity range for V up to 1000 m/s [19]. M_0 is impact speed Mach number defined by V/C_0. Both the aforementioned formulas give the hydraulic pressure without the consideration of the solid compressibility and thus may only be reasonable in liquid-rigid plate impact. If the elastic deformation of the solid is involved, the impulsive pressure yields to Engel's approximation [20],

$$P_{\mathrm{H}} = \rho_0 C_0 V \frac{1 + kM_0}{1 + \lambda(1 + kM_0)} \tag{3}$$

in which λ refers to the acoustic impedance ratio between the liquid and the solid, defined as

$$\lambda = \frac{\rho_0 C_0}{\rho_{\mathrm{s}} C_{\mathrm{s}}} \tag{4}$$

where ρ_{s} and C_{s} are the density and the shock wave speed of the solid respectively. Engel's equation is only valid for homogenous materials since constant values of ρ_{s} and C_{s} are assumed. For the anisotropic material CFRP laminate in the present study, C_{s} is direction-dependent. As the impact direction is along the thickness, the 3-direction elastic modulus E_{33} is utilized to determine the average wave speed of CFRP, defined by [21]

$$C_{\mathrm{s}} = \sqrt{\frac{E_{33}}{\rho_{\mathrm{s}}}} \tag{5}$$

When the shock wave speed exceeds the contact periphery, the stage of water-hammer pressure will be terminated, with the whole duration expressed as [22],

$$\tau = \frac{3RV}{2C_l^2} \tag{6}$$

in which R refers to the radius of curvature of the liquid front and C_l represents the shock wave speed of the liquid, which is related to its sound speed C_0 by,

$$C_l = C_0 + kV \tag{7}$$

After that, the compressed liquid is discharged and a high-speed liquid jet is ejected laterally along the solid surface, shown in Fig. 1 (b). The velocity of the lateral jet is generally two to six times of the initial impact velocity [23], and the high pressure at the surface gradually releases and reduces to the much lower Bernoulli stagnation pressure, defined as [24]

$$P_{\mathrm{i}} = \frac{\rho_0 V^2}{2} \tag{8}$$

3. Experiment method

The waterjet generating facility used in this study is developed based on the principles of Single impact waterjet apparatus (SIJA) in

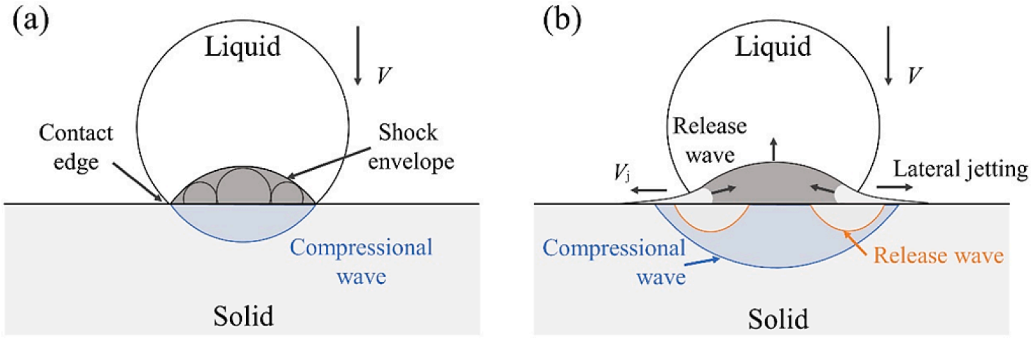

Fig 1. Liquid-solid impingement. (a) Liquid compression. (b) Lateral jetting.

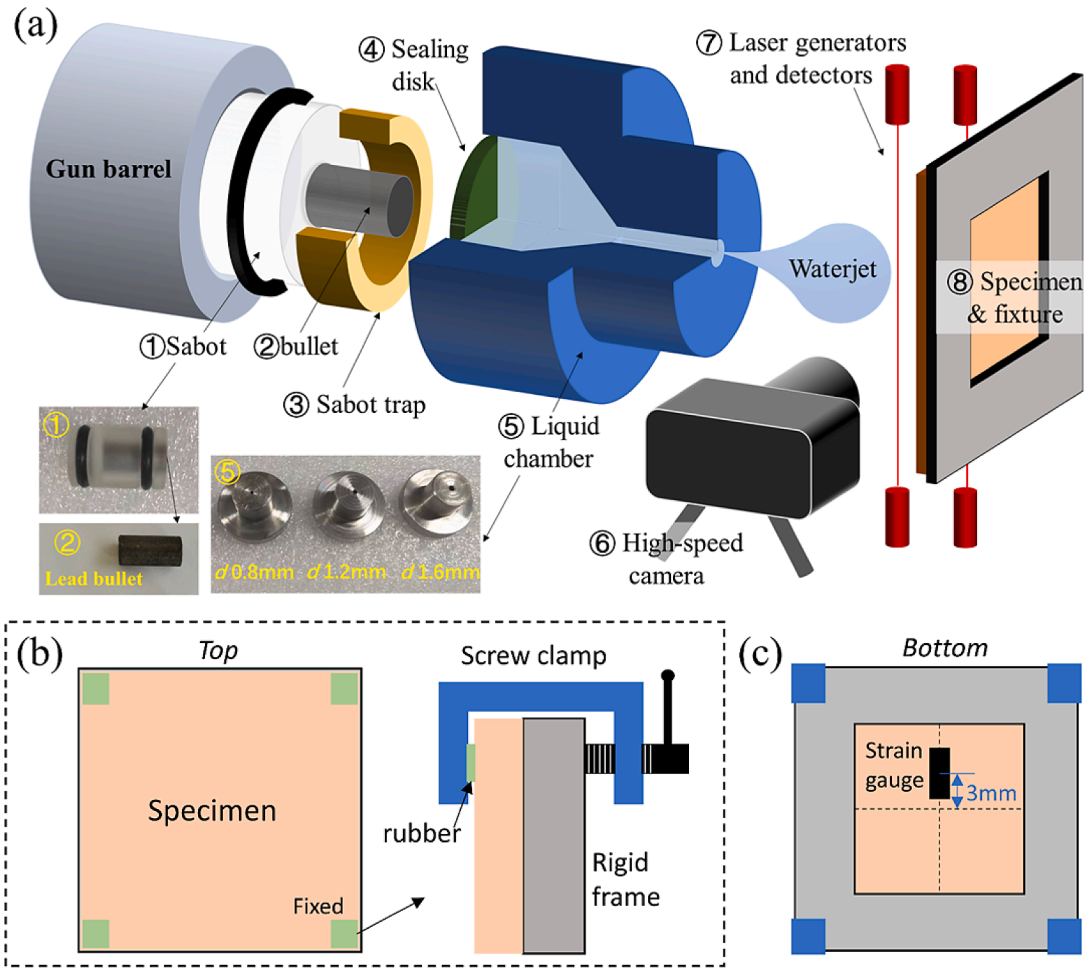

Fig 2. (a) Waterjet generating experiment apparatus, (b) clamping method of the specimen and (c) location of the strain gauge.

Cavendish Laboratory [5]. The schematic of the whole apparatus is shown in Fig. 2(a). Before the test, a stainless-steel chamber with a converging nozzle is filled with tap water and sealed by a neoprene disc. Then a bullet is accelerated down the barrel and impinged onto the sealing disc, propelling the liquid to eject and thus forming a high-speed waterjet. The velocity of the waterjet is measured by recording the interval of interrupting two laser beams. The morphological changes of the moving waterjet are captured by a high-speed camera Phantom V711, with images of 128*128 resolution taken at intervals of 4.76 μs. Stand-off distance (SOD), referring to the distance between the waterjet nozzle and the specimen, is set to be 10mm in this study, where the shape and velocity of waterjets reach a stable state as reported in [25,26]. This facility can generate stable and repeatable waterjets with the speed between 100 to 700m/s and the diameter between 4 to 7mm. Different waterjet velocities are realized by adjusting the pressure of the propelling gas and different waterjet diameters are obtained by using reservoirs with different orifice diameters.

The CFRP laminates used in present tests were manufactured from a unidirectional carbon-fiber/epoxy prepreg T700/7901. The material parameters are listed in Table 1. The final specimen with the stacking sequence of $[0,90]_{2s}$ has the dimensions of 28mm × 28mm and 1.2mm in thickness. Before test, the top surface of the CFRP is carefully grinded by sandpapers of 3000 grit and polished by 1um diamond paste before test, in order to get a good smooth initial surface and hence minimize the influence of surface asperities on damage results [27,28]. In the test, the CFRP specimen was fixed on a rigid frame with a square back hole of 16mm in length and width by four screw clamps at the corners (shown in Fig. 2(b)), with small pieces of rubber pad placed between the clamp and the specimen to reduce the stress concentration near the clamping ends. The top surface of the specimen was perpendicular to the waterjet impacting direction. Strain history was measured by a strain gauge attached along the transverse direction, 3mm from the center of the back surface with the marking diagram shown in Fig. 2(c). Specimens after tests were observed by a stereo microscope for evaluating the surface damage dimensions. A stylus profile-meter was used to measure the profile of the impacted surface and ultrasound C-scan devices were employed to inspect their internal defects.

Table 1
Material properties of the carbon-fiber/epoxy unidirectional laminate [29,30].

Property	Value
Density	ρ=1600 kg/m^3
Elastic properties	E_{11}=115GPa, E_{22}=E_{33}=9GPa, G_{12}=G_{13}=4.8GPa, G_{23}=3.8GPa, ν_{12}=ν_{13}=0.3, ν_{23}=0.35
Strength	X_t=2300MPa, X_c=1050MPa, Y_t=42MPa, Y_c=143MPa, S_{12}=S_{13}=S_{23}=116MPa
Fracture toughness	G_{ft}=133N/mm, G_{fc}=40N/mm, G_{mt}=0.6N/mm, G_{mc}=2.1N/mm

4. Numerical modelling

4.1. Finite element model

The whole numerical model is comprised of three components shown in Fig. 3. The plate is composed of 8 unidirectional plies stacked in the

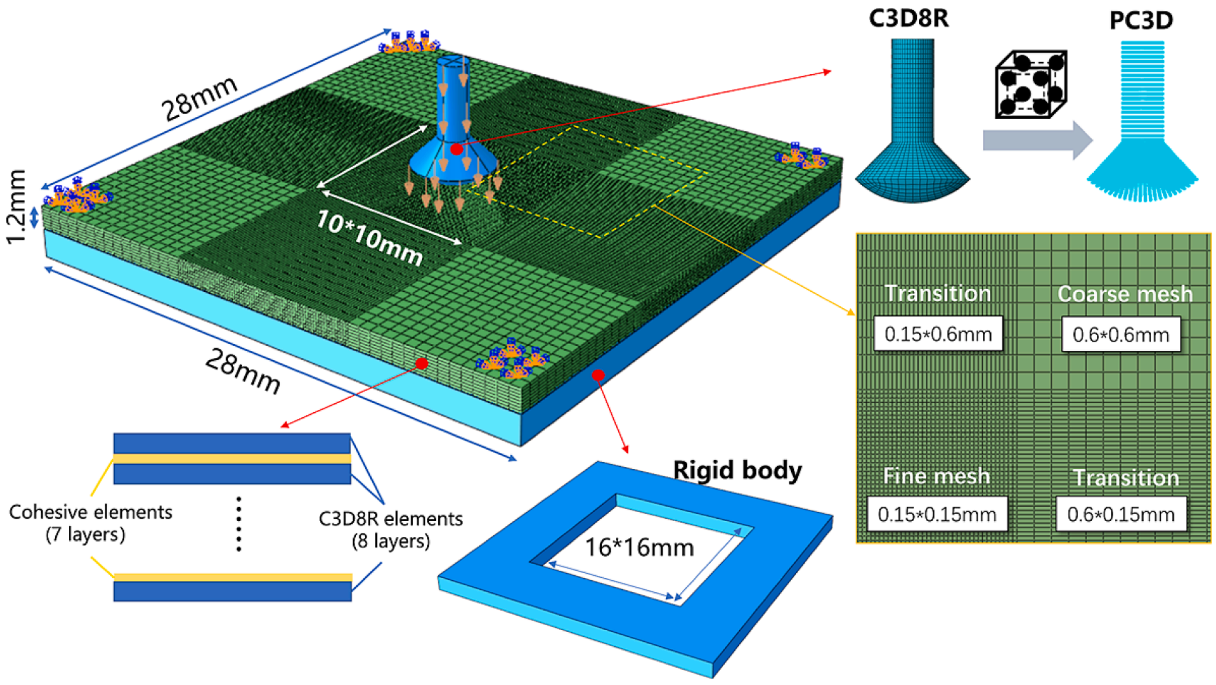

Fig 3. Finite element model of waterjet-CFRP laminate impact event

sequence of $[0,90]_{2s}$ and each ply has one layer of elements with the ply thickness of 0.15mm. 8-node reduced integration brick element (C3D8R) is selected to mesh all the laminae. Cohesive elements (COH3D8) are inserted between neighboring plies to describe the behavior of the interlaminar interface, with the interface thickness of 0.01mm. After mesh convergence study, the central local area (10 × 10mm) of the plate is assigned to a refined mesh size (0.15 × 0.15mm) for the accurate calculation near impacted region, while a coarser mesh (0.6 × 0.6mm) is applied to the rest of the plate to reduce the required CPU time. There are four transition areas with the medium mesh (0.15 × 0.6mm) for two reasons. One is to achieve good transition from fine mesh to coarse mesh without sharp corner angles of elements. The other is due to the possible extension of interlaminar delamination outside the fine-mesh region. It has been observed in experiment results that the scope of the internal damage could be several times larger than that of the surface damage (which will be shown in Fig. 6). Therefore, the medium mesh is assigned to the cross region to capture the integrated scope of the delamination in cohesive layers. The similar meshing scheme was also applied in finite element model of waterjet-solid impact in [17]. The prediction of all the intralaminar damage behaviors presented in Section 4.2.1 is realized by VUMAT subroutines. The constitutive model of the cohesive elements presented in Section 4.2.2 has been embedded in Abaqus/explicit codes for the convenience of simulating interlaminar delamination. The movement of a waterjet is calculated by Smooth particle hydrodynamics (SPH) method [31] embedded in Abaqus 6.14. Instead of a grid, SPH particles are interacted with each other following a kernel interpolation within a smoothing length, thus avoiding severe mesh distortion during large deformation. The waterjet is modelled by solid elements in advance and these "parent" elements are converted to SPH particles (PC3D) at the beginning of the analysis. The interaction of the two parts is calculated by general contact algorithm. Its back surface is mounted on the rigid fixture with hard contact, and some nodes near the edge of the front surface are fixed to constrain the through-thickness displacement of the plate. Abaqus/Explicit analysis is applied to solve the whole impact event with a total time of 30 μs, which is a duration long enough for the flow to reach a steady state.

4.2. Composite damage model

4.2.1. Intralaminar damage model

4.2.1.1. Stress-strain relationship with damage variables. In a composite laminate, each lamina can be regarded as a transversely isotropic material, of which there are five independent elastic parameters for an undamaged lamina. When further loading is exerted beyond capacity, the lamina will start to damage with cracks accumulating, leading to the degradation of the mechanical properties. The damaged stiffness matrix applied in this study refers to Li et al. [30] and is given by

$$C_{\mathrm{d}} = \frac{1}{\Delta}\begin{bmatrix} d_{\mathrm{f}}E_{11}(1-d_{\mathrm{m}}\nu_{23}\nu_{32}) & d_{\mathrm{f}}d_{\mathrm{m}}E_{11}(\nu_{21}+\nu_{23}\nu_{31}) & d_{\mathrm{f}}E_{11}(\nu_{31}+d_{\mathrm{m}}\nu_{21}\nu_{32}) & & & \\ & d_{\mathrm{m}}E_{22}(1-d_{\mathrm{f}}\nu_{13}\nu_{31}) & d_{\mathrm{m}}E_{22}(\nu_{32}+d_{\mathrm{f}}\nu_{12}\nu_{31}) & & & \\ & & E_{33}(1-d_{\mathrm{f}}d_{\mathrm{m}}\nu_{12}\nu_{21}) & & & \\ & & & \Delta d_{\mathrm{f}}d_{\mathrm{m}}G_{12} & & \\ & & & & \Delta d_{\mathrm{f}}d_{\mathrm{m}}G_{23} & \\ & & & & & \Delta d_{\mathrm{f}}d_{\mathrm{m}}G_{13} \end{bmatrix} \tag{9}$$

in which

$$\begin{cases} d_f = (1-d_{ft})(1-d_{fc}) \\ d_m = \max\left((1-S_{mt}d_{mt})^2, (1-S_{mc}d_{mc})^2\right) \\ \Delta = 1-d_f d_m \nu_{12}\nu_{21} - d_m\nu_{23}\nu_{32} - d_f\nu_{13}\nu_{31} - 2d_f d_m \nu_{21}\nu_{32}\nu_{13} \end{cases} \tag{10}$$

where d_f and d_m represent the fiber and matrix damage variables respectively, and d_{ft}, d_{fc}, d_{mt}, d_{mc} are the damage variables for fiber and matrix damage under tensile and compression loads (detailed calculation elaborated in Section 4.2.1.3). The coefficients S_{mt} and S_{mc} aim to control the shear stiffness degradation due to matrix damage in tension and compression, with the values are assigned to 0.9 and 0.5 respectively.

4.2.1.2. Damage initiation. Since little fiber damage occurred in liquid impact tests of this study, maximum stress criteria are applied to diagnose the initiation of fiber tension and compression damage. Hou failure criteria [32] are proposed for predicting the onset of the matrix tension and compression damage.

$$\text{Fibertensilefailure}(\sigma_{11} \geq 0) r_{ft} = \left(\frac{\sigma_{11}}{X_t}\right)^2 \tag{11}$$

$$\text{Fibercompressionfailure}(\sigma_{11} < 0) r_{fc} = \left(\frac{\sigma_{11}}{X_c}\right)^2 \tag{12}$$

$$\text{Matrixtensilefailure}(\sigma_{22} \geq 0) \quad r_{fc} = \left(\frac{\sigma_{22}}{Y_t}\right)^2 + \left(\frac{\sigma_{12}}{S_{12}}\right)^2 + \left(\frac{\sigma_{23}}{S_{23}}\right)^2 \tag{13}$$

$$\text{Matrixcompressionfailure}(\sigma_{22} < 0) r_{fc} = \frac{1}{4}\left(\frac{-\sigma_{22}}{S_{12}}\right)^2 + \frac{Y_c^2\sigma_{22}}{4S_{12}^2 Y_c} - \frac{\sigma_{22}}{Y_c}\left(\frac{\sigma_{22}}{S_{12}}\right)^2 \tag{14}$$

Here X_t, X_c, Y_t, Y_c denote tensile and compression strengths along and perpendicular to fiber orientations. S_{12} and S_{23} refer to the in-plane and out-of-plane shear strength respectively. The variables r_{ft}, r_{fc}, r_{mt}, r_{mc} are the failure criterion values for fiber and matrix damage under tensile and compression loads.

4.2.1.3. Damage evolution. Progressive degradation method [33] is proposed to describe the degraded loading capacity of a damaged material based on the theory of the continuum damage mechanics (CDM). In this study, a linear degradation trend is applied and the damage evolution starts with the stiffness matrix is softened when the failure criterion is satisfied. Equivalent displacement method based on element fracture energy is adopted here to calculate the damage variables aforementioned in Section 4.2.1.1. The evolution of damage variables for each failure mode I is expressed as

$$d_I = \frac{\delta_{I,eq}^f\left(\delta_{I,eq} - \delta_{I,eq}^0\right)}{\delta_{I,eq}\left(\delta_{I,eq}^f - \delta_{I,eq}^0\right)} \quad (d_I \in [0,1], I = ft, fc, mt, mc) \tag{15}$$

$$\delta_{I,eq}^f = \frac{2G_I}{\sigma_{I,eq}^0}, \quad \delta_{I,eq}^0 = \frac{\delta_{I,eq}}{\sqrt{r_I}}, \quad \sigma_{I,eq}^0 = \frac{\sigma_{I,eq}}{\sqrt{r_I}} \tag{16}$$

in which $\delta_{I,eq}^0$ and $\sigma_{I,eq}^0$ denote the equivalent displacement and equivalent stress at the damage onset respectively, and $\delta_{I,eq}^f$ is the equivalent displacement when the material loses all loading capacity and totally fails. r_I is the failure criterion value and G_I refers to the fracture energy of failure mode I. The detailed formulas of the equivalent displacement $\delta_{I,eq}$ and equivalent stress $\sigma_{I,eq}$ of each failure mode are given in [30].

4.2.2. Interlaminar damage model

Delamination is a major failure mode in impact damage of a composite laminate. Cohesive elements are implemented in the present study to describe the interlaminar delamination damage. The constitutive model of cohesive elements is based on a bilinear traction-separation law [34], relating the interlaminar traction stress (T_n, T_s, T_t) to the separation displacement between the nodes at the interface of adjacent plies. The elastic mechanical behavior of cohesive elements is defined by penalty stiffness corresponding to normal and two shear directions (K_{nn}, K_{ns}, K_{st}). Here the quadratic nominal stress criterion is applied to judge the onset of delamination, in which T_n^0, T_s^0, T_t^0 represent the normal and two shear strengths at the interface.

$$\frac{\langle T_n\rangle^2}{\left(T_n^0\right)^2} + \frac{T_s^2}{\left(T_s^0\right)^2} + \frac{T_t^2}{\left(T_t^0\right)^2} = 1 \tag{17}$$

Once the failure criterion in the above equation reaches the threshold, the Benzeggagh and Kenane (B-K) criterion [35] is implemented to predict the damage evolution of delamination by coupling the critical fracture energies of the three failure modes (G_n^c, G_s^c, G_t^c). η is a material constant in the B-K formula.

$$G^c = G_n^c + \left(G_s^c - G_n^c\right)\left\{\frac{G_S}{G_T}\right\}^\eta, G_S = G_s + G_t, G_T = G_n + G_s + G_t \tag{18}$$

in which G_n, G_s, G_t denotes the work done by the tractions and their relative displacements in the normal and two shear directions and G_T is the sum of the three. The material parameters of cohesive elements in this study are listed in Table 2.

4.3. Modelling of the waterjet

In order to simulate the test conditions, the geometric model of the waterjet is established by imitating its profiles in tests. Key dimensional features are extracted from the typical shapes of the waterjets with different diameters. Therefore, a waterjet model is regarded as a combination of a spherical crown, frustum of a cone and a cylinder. The frontal radius of the crown (R) refers to the radius of the waterjet, and the diameter of the cylinder (D) equals to that of the orifice. The overall length (L) is set to twice the crown radius R. Assuming the profiles of waterjets do not change with their velocities, three numerical models of waterjets with different diameters (4.8mm, 5.5mm and 6.2mm) are displayed in Fig. 4.

Mie-Gruneisen Equation of state (EOS) is available in ABAQUS/Explicit code for the description of the hydrodynamic behavior of water. Here the linear U_s–U_p Hugoniot form of Mie-Gruneisen EOS is presented, with the detailed derivation referred to [17].

$$p = \frac{\rho_0 C_0^2 \varphi}{(1-s\varphi)^2}\left(1 - \frac{\Gamma_0\varphi}{2}\right) + \Gamma_0\rho_0 E_m \tag{19}$$

In the above equation, Γ_0 is a Gruneisen material constant and ρ_0 is the reference density. φ is the nominal volumetric compressive strain defined by $1 - \frac{\rho_0}{\rho}$. C_0 and s are introduced to define the linear relationship between the linear shock velocity U_s and the particle velocity U_p, as follows

$$U_s = C_0 + sU_p \tag{20}$$

Table 2
Material properties of the interface cohesive element [29,30].

Property	K_{nn} (GPa/mm)	K_{ns} (GPa/mm)	K_{st} (GPa/mm)	T_n^0 (MPa)	T_s^0 (MPa)	T_t^0 (MPa)	G_n^c (N/mm)	G_s^c (N/mm)	G_t^c (N/mm)	η
Value	100	100	100	20	36	36	0.6	2.1	2.1	1.45

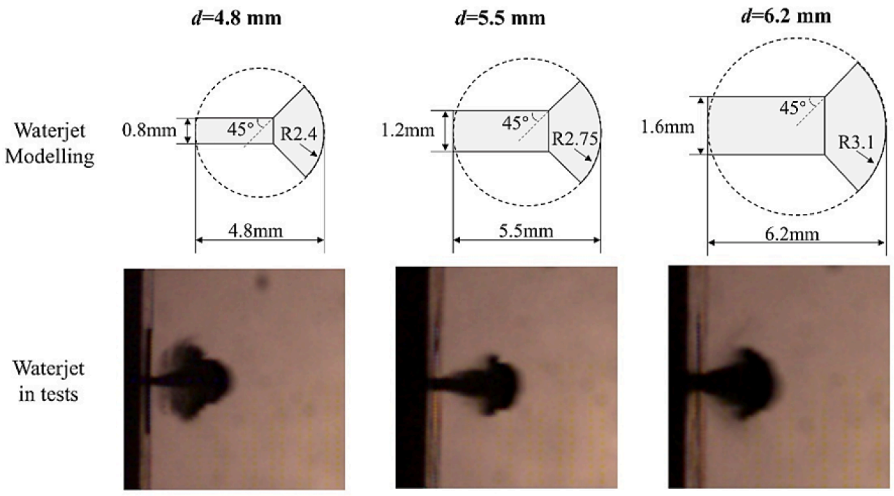

Fig 4. Modelling of waterjets with three different diameters

Table 3
Material properties of the water in Mie-Gruneisen EOS.

Property	ρ_0(kg/m^3)	C_0(m/s)	s	Γ_0
Value	1000	1489	1.79	1.65

The values of the coefficients for water are referred to [36] and listed in Table 3.

5. Results and discussion

5.1. Water-hammer pressure

Fig. 5(a) illustrates the time history of the contact pressure at the center point on the surface of the CFRP plate impacted by a waterjet with the diameter of 6.2mm and the velocity of 557m/s. Results show that the transient pressure reaches the peak (1.03 GPa) at the first instant of contact, followed with the relatively low stagnation pressure dominated by the length of the water column. Though there are numerical oscillations in simulation results (represented by the black solid line), the peak contact pressure and average steady pressure are fairly in line with the approximation of Eq. (3) for the 1-D water-hammer pressure and Eq. (8) for the stagnation pressure (depicted by the red dotted line) respectively.

It is revealed in Fig. 5(b) that the pressure distribution is non-uniform along the central path of the impacted surface. The critical location with the maximum pressure appears not at the center point but about 1.5mm away from the center at 1μs, because of the successive accumulation of a bunch of wavelets before the shock envelope overtakes the expanding contact edge. Though the value of the peak pressure

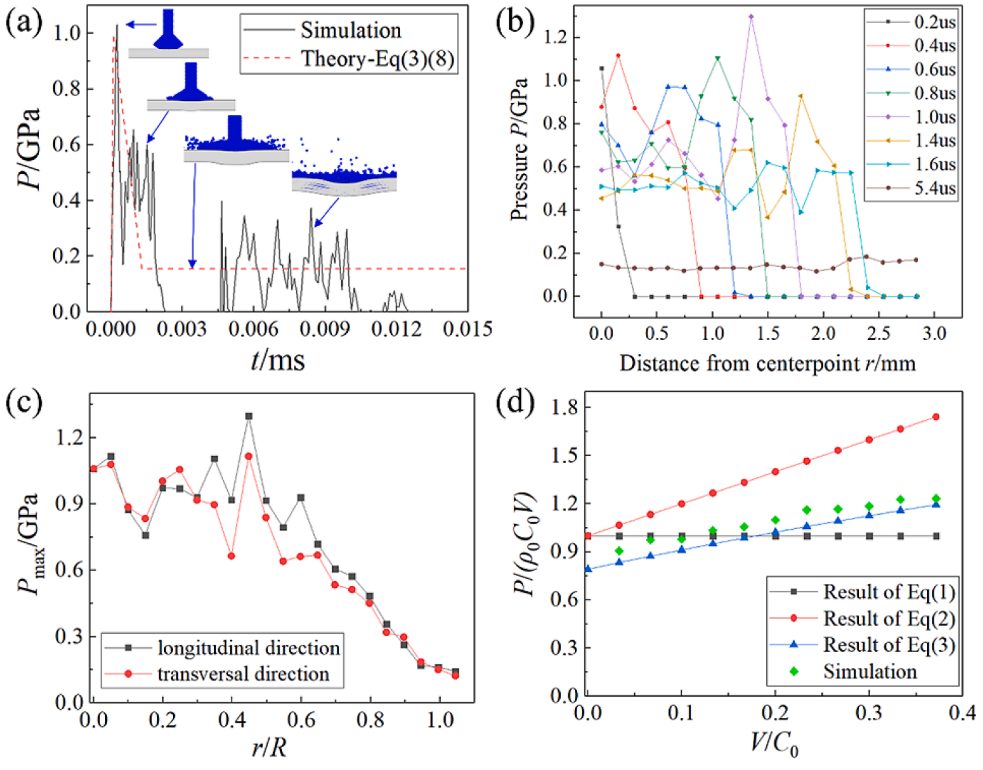

Fig 5. Simulation results of water-hammer pressure. (a) Time history of the water-hammer pressure of the center point on the CFRP surface impacted by a waterjet with the velocity of 557m/s and the diameter of 6.2mm. (b) Variation of the pressure distribution of the impacted surface as time progresses. (c) Maximum contact pressure distributed along both the longitudinal and transverse directions. (d) Normalized results of the peak impact pressure of the center point with respect to the impact velocity

is underestimated compared to the results of previous investigations (around $3\rho_0 C_0 V$), this high pressure lasts a very short time (several nanoseconds) and thus is generally believed to have little influence on the material damage. After this peak pressure releases and the water-hammer phase is finished, the pressure within the contact area gradually reduces and is eventually evenly-distributed with Bernoulli stagnation pressure.

Fig. 5(c) demonstrates the maximum contact pressure P_{max} distributed along both the longitudinal and transverse directions. The radial location is normalized using the true distance from the center point r divided by the radius of the waterjet R. Results show that P_{max} initially fluctuates with the radial location increasing while it gradually decreases after r/R exceeds 0.5. The exact values of P_{max} are a little higher along x direction than y direction while the changing tendencies are identical. This implies the condition that the stress distribution may not be uniform within the contact area due to the anisotropic mechanical properties of the CFRP laminate. More intuitive knowledge can be found in the surface contour plot in Section 5.2.

In Fig. 5(d), three empirical formulas presented in Section 2 are chosen as a reference to evaluate the simulation results of the peak impact pressure with respect to the impact velocity. The dimensionless pressure is expressed as the true pressure P divided by water-hammer pressure $\rho_0 C_0 V$, and the impact velocity is normalized to be the ratio of V/C_0. It is illustrated that Eq. (1) presents a constant dimensionless pressure in spite of the velocity variation, since the solid is regarded as rigid material and the sound speed of liquid is constant (i.e. the compressibility is not considered for both the solid and the liquid). When the compressibility of the liquid is introduced by the parameter k, Eq. (2) gives a linear increasing trend with the velocity rising, and the approximation of the water-hammer pressure apparently increases compared to the results of Eq. (1). As for Eq. (3), the compressibility is additionally incorporated for the solid by introducing another parameter λ, while the calculating results are found to be reduced compared with Eq. (2). Compared with the simulation results, Eq. (3) provides the best estimation especially at higher speeds while Eq. (1) can generally predict the cases with low impact speeds (V/C_0<0.15). All the above discussions point to the fact that the compressibility of the liquid elevates the water-hammer pressure while the compressibility of the solid alleviates it. The two factors may exert little influence at low speeds which leads to a simple expression as Eq. (1), but both of them cannot be neglected when the impact speed is relatively high (mostly exceeding 250m/s) and thus Eq. (3) is recommended.

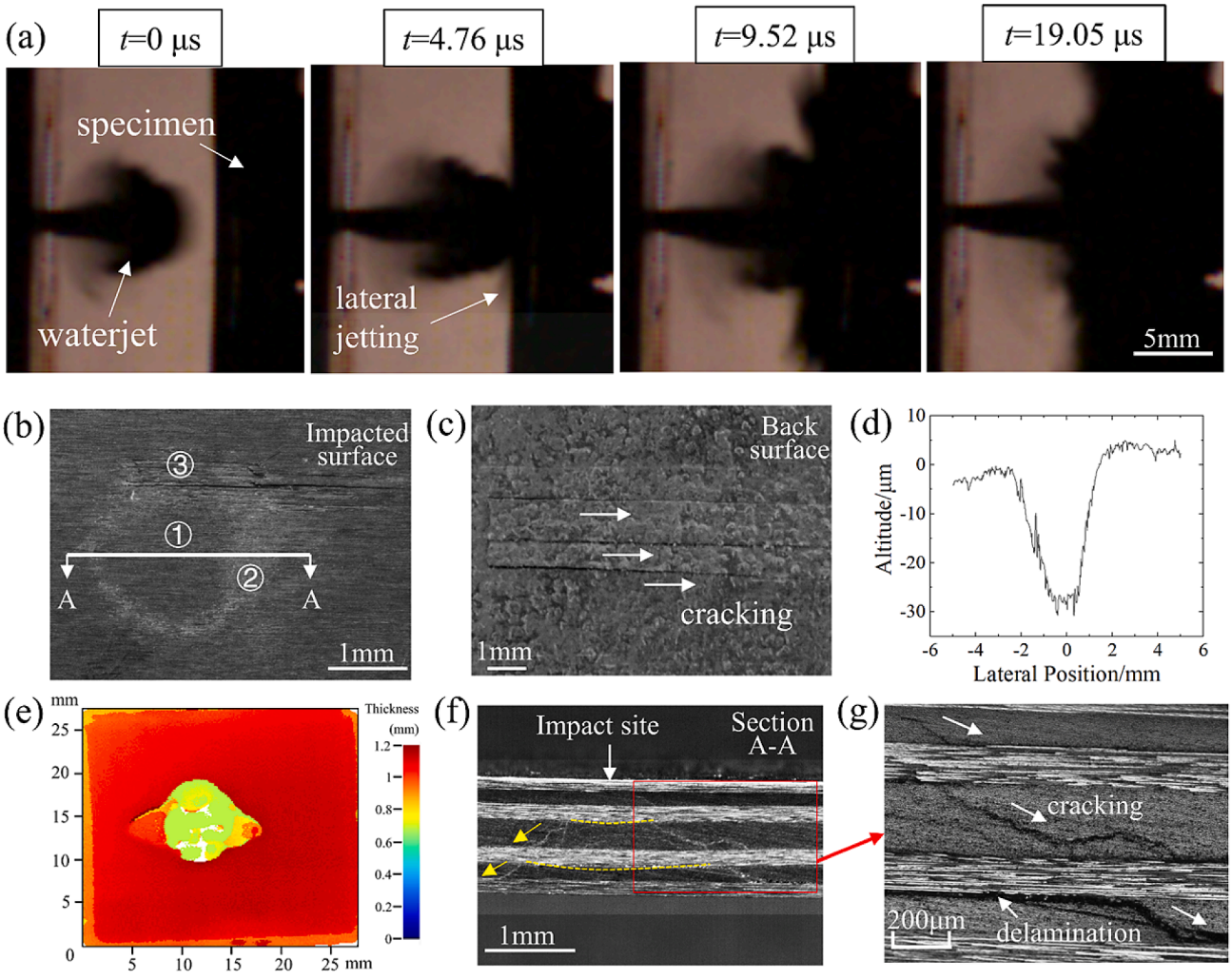

Fig 6. Experiment results of CFRP laminate impacted by a waterjet with the velocity of 557m/s and the diameter of 6.2mm. (a) High-speed photographic recording of the impact process. (b) Micrograph of the impacted surface and (c) the back surface. (d) Surface profile of the impact location. (e) C-scan result of the impacted specimen. (f) Micrograph of the cross-section perpendicular to the surface and (g) its local magnification.

5.2. Dynamic response and damage patterns of the CFRP laminate subjected to waterjet impact

The experiment results of a CFRP specimen impacted by a waterjet with the diameter of 6.2mm and the velocity of 557m/s are demonstrated in Fig. 6. The impact process is recorded by high-speed photography in Fig. 6(a) that the lateral jetting can be observed clearly, while after that the boundary between the waterjet and the specimen is hard to be distinguished since both of them are opaque. In the micrograph Fig. 6(b), typical damage patterns of the impacted surface are composed of a center region with no visible surface damage (shown at ①) and an annular faded "failure ring", in which there are resin removal(②), matrix cracking(③) and sometimes minor fiber breakage. At the back surface, there are an array of cracks parallel to the fiber direction shown in Fig. 6(c). Fig. 6(d) displays the measured profile of the impacted surface along the solid line in Fig. 6(b) and a shallow U-shaped pit is observed, indicating that permanent deformation occurred on the CFRP specimen. C-scan result in Fig. 6(e) depicts a diamond-shaped delamination inside the laminate, and the damaged region clearly presents unequal feature, with the extension larger along longitudinal direction than the transverse direction. In the cross-section view shown in Fig. 6(f), visible deformation can be noticed in several plies beneath the impact site, together with the matrix cracking extending away from the impact site and interlaminar delamination. After partial magnification in Fig. 6(g), macroscopic cracks are presented in matrix throughout the lamina, with the increasing width and scope from top to bottom, connecting the delamination of the two adjacent layers.

Fig. 7 shows the framing sequences of the jet impacting on a CFRP target with contour plots of the velocity variation throughout the waterjet, Mises equivalent stress and contact pressure over the impacted surface at 6 instants between 0 and 30μs. At the first snapshot, the waterjet impacts the CFRP plate causing a transient high pressure and

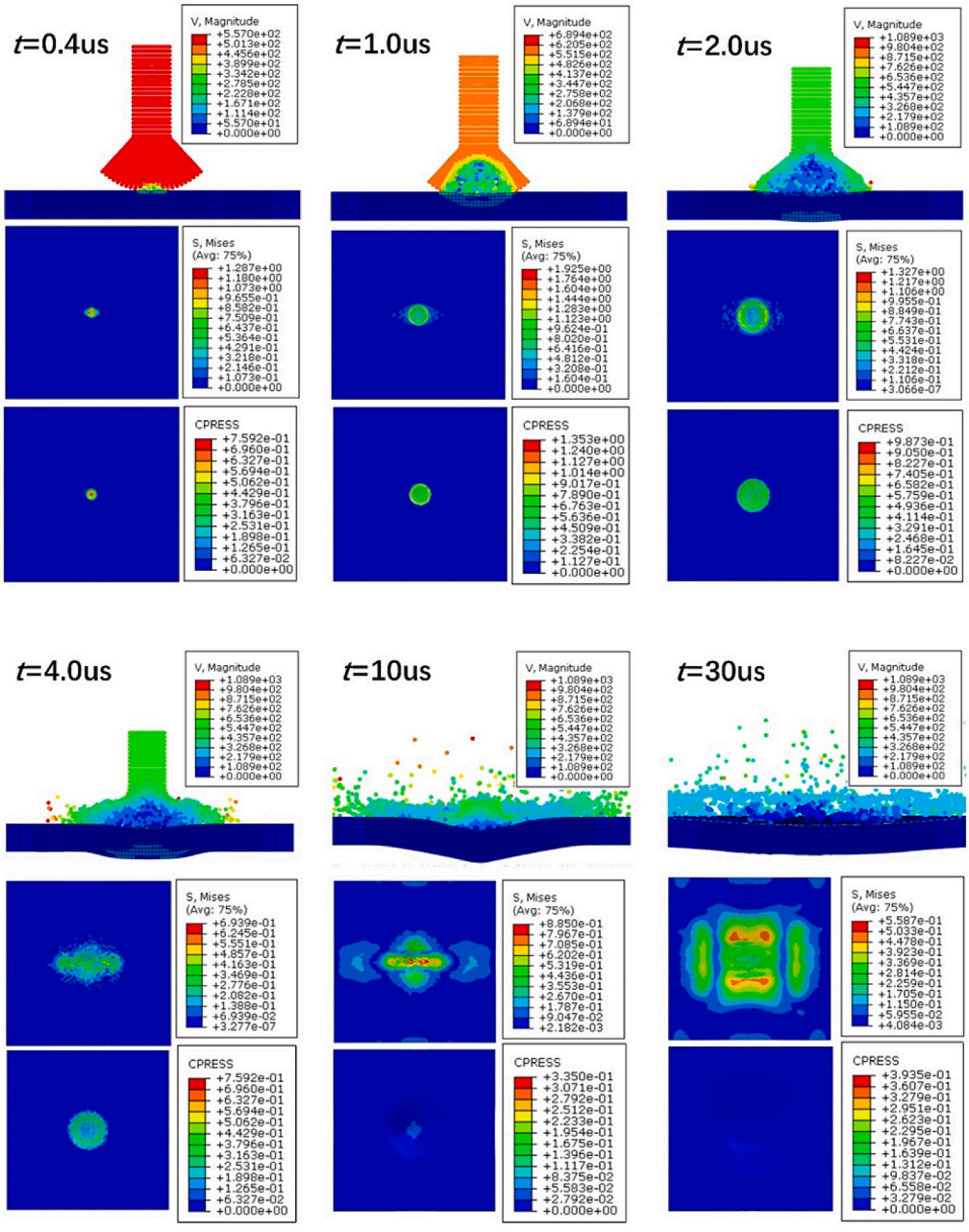

Fig 7. Contour plots of the velocity throughout the waterjet (the top photo at each moment, with the unit of m/s), Mises equivalent stress (middle, GPa) and contact pressure (bottom, GPa) over the impacted surface at 6 instants.

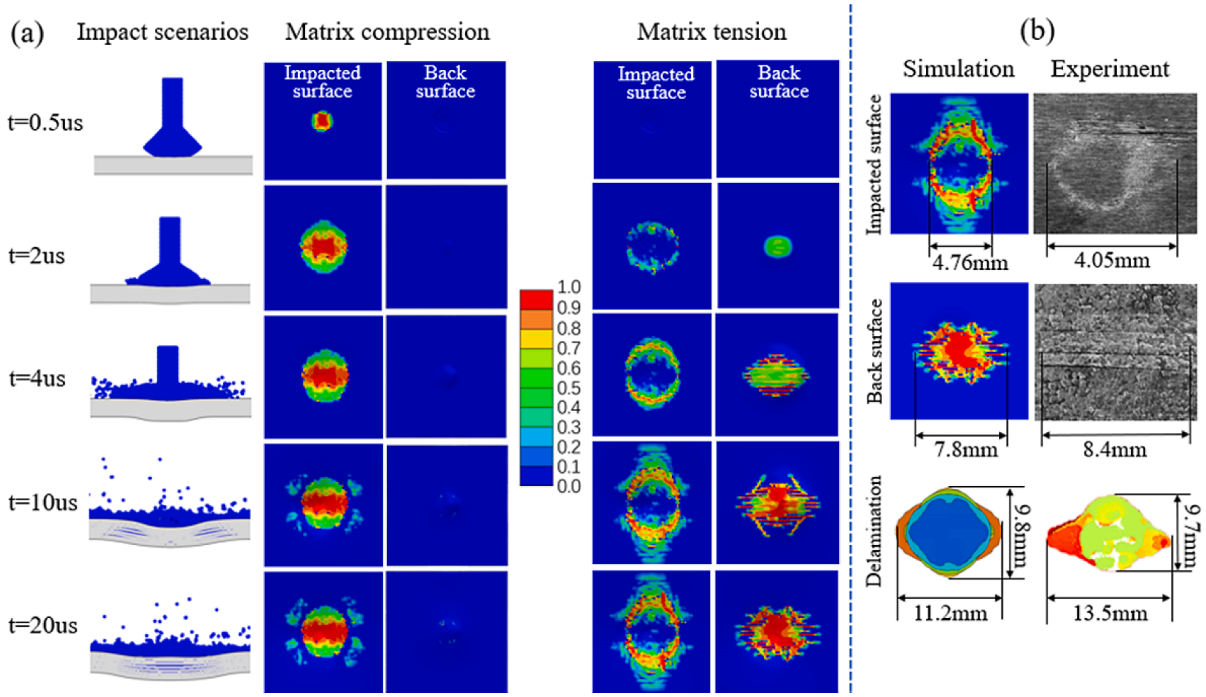

Fig 8. (a) Simulation results of the damage evolution of matrix compression and tension at the impacted and back surface. (b) Comparison of damage patterns in simulation and experiment.

the affected water particles slow down within the shock envelope until the lateral jetting is about to occur at 1μs. When the jetting starts, the water SPH particles are accelerated at the contact periphery and reach the peak velocity of 1089m/s (about twice the impact velocity) at 2μs. Subsequently, the waterjet continues to interact with the target and flow along the surface with a relatively low pressure lasting for about 20μs. When the whole water impact loading is over, the deformed target will rebound to some extent and oscillate due to the propagation and reflection of the stress waves. It is noteworthy that the Mises stress generated on the surface along the longitudinal direction is larger than that along the transverse direction, while such feature is not observed in contact pressure. Both the maximum Mises stress and contact pressure occur at t=1μs when the shock wave of water is about to overtake the contact boundary, and the elements with maximum values are also at the location of the contact boundary (i.e. about 1.35mm from the impact center).

Fig. 8(a) exhibits major damage modes and their evolution on the surface of CFRP specimen during the waterjet impingement. There is no fiber failure occurred, so the intralaminar failure only incorporates matrix compression damage and matrix tension damage. In the damage contour plots, the region marked in blue represents no damage (denoted as 0 in the legend) and somewhere in red indicates complete failure (denoted as 1). Visually, matrix compression damage is observed to initiate at the instant of contact and keep expanding during the stage of the water-hammer pressure. After the shock wave surpasses the contact edge, the area of the matrix compression damage remains substantially constant on the impacted surface. On the contrary, matrix tension damage has not occurred until the onset of lateral jetting and the damage scope is broadened as the rear water column continues to exert a long duration of stagnation pressure on the surface. Though there is no matrix compression failure on the back surface, the matrix tension damage is obviously emerged when the compression wave reflects at the back surface and continuously deteriorated due to the propagation of stress waves. Compared with the experiment results in Fig. 8(b), the annular matrix tension damage resembles the “failure ring” on the top surface with similar diameters. An array of longitudinal cracks is observed on the back surface in both simulation and experiment. The projected areas of interlaminar delamination in simulation and test are observed to resemble each other in terms of the diamond shape and its dimensions. The matrix compression failure caused by water-hammer pressure leads to the permanent deformation near the impact location. The altitude of the crater after impact is quantitively displayed in Fig. 9 (a), in which the simulation result shows good agreement with that in experiment. The time history of the strain at the back surface (the specific location shown in Fig. 2(c)) is also compared in Fig. 9(b) the and the results are similar in both the peak and the amplitude. The consistency of all the above results further proves the reasonability of the numerical methods applied in this study.

Fig. 10 displays the two types of intralaminar damage in each layer and the interlaminar delamination between all the adjacent layers. Results show that the matrix tensile damage area gradually extends to be larger from the upper to the lower layers (except the first layer), while the matrix compression damage reduces its scope from top to bottom. There is even no matrix compression damage detected near the back three layers. This phenomenon is also reported in results of low-velocity impact by a rigid impactor [30,37] and the explanations are presented as follows. Matrix compression damage firstly appears on the top layer due to the hydraulic shock exerted on the surface at the instant of impact, and then the compression damage expands to lower layers through the thickness with the propagation of compression stress wave. On the other hand, matrix tensile damage usually initiates at the bottom layer due to the reflection of the compression wave at the back surface, and propagates to the upper layers with the release wave. It is important to add that the occurrence of lateral jetting aggravates the extents of matrix tensile damage on the first layer. The presented damage shapes of the interlaminar delamination are composed of the cohesive elements with their damage variables exceeding 0.8, while the contour plot on them represents a built-in output variable MMIXDME in Abaqus/Explicit. Since the mixed fracture energy criterion is used in this study, the mode mix ratio m_1 is introduced to quantify the relative proportions of normal and shear fracture modes, defined by

$$m_1 = \frac{G_n}{G_T} \tag{19}$$

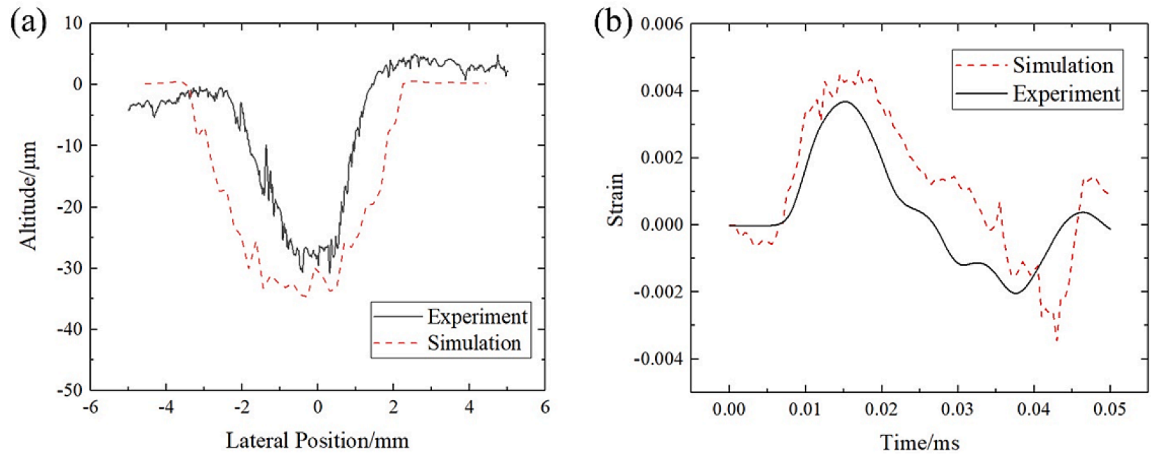

Fig 9. Simulation and experiment results of (a) profile of the impacted location and (b) time history of the strain at the back surface.

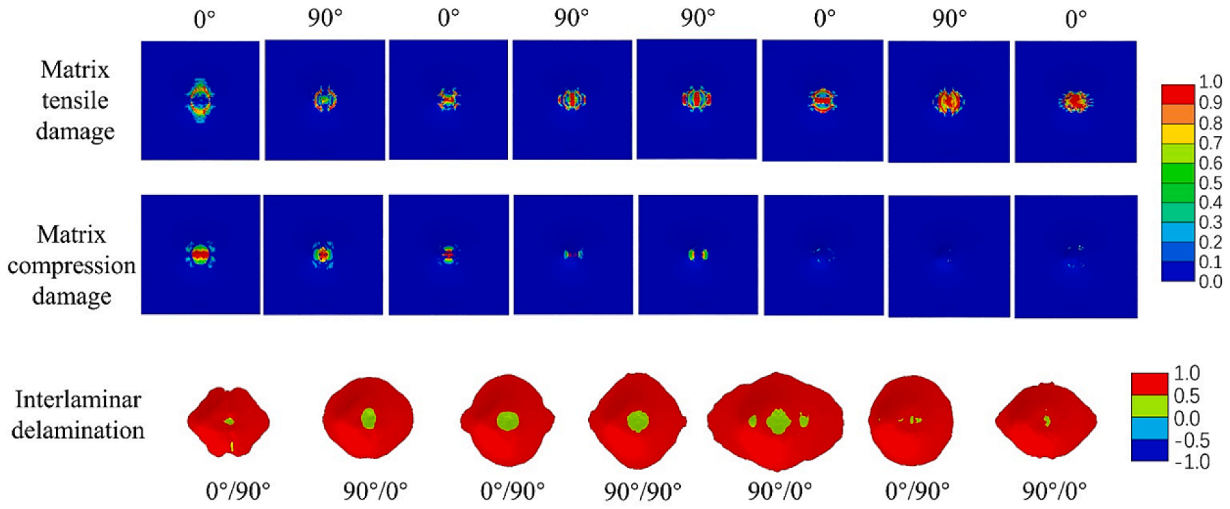

Fig 10. Matrix tensile and compression damage in each layer and interlaminar delamination between all the adjacent layers.

in which G_n and G_T have been defined in Section 4.2.2. The variable MMIXDME measures the fraction of the total deformation that is shear during damage evolution, evaluated by 1-m_1 and set to -1 before initiation of damage. When MMIXDME equals to 0 or 1, respectively, the element is failed by totally normal fracture or totally shear fracture. Therefore, a failed element is dominated by normal fracture if the value of MMIXDME in the range of 0 to 0.5 while a shear-dominated fracture is indicated when it goes from 0.5 to 1.0. It is clearly observed that the interlaminar delamination of all interfaces is dominated by shear fracture except for a central small region dominated by normal fracture.

5.3. Parameter studies

The present section will evaluate the effects of the velocity and diameter of the waterjets on the damage extents of CFRP laminates according to the five damage measuring parameters D_2, D_1, L_x, L_y, S_{xy}. The surface damage size D_2 represents the minimum diameter of the central no-visible-damage zone, and D_1 represents the outermost diameter of surface "failure ring". The internal damage dimension L_x and L_y represents the longitudinal and the transverse maximum lengths of the delamination zone respectively, and S_{xy} represents the projected area of the delamination zone from top to bottom measured by C-scan devices.

Fig. 11 depicts the results of different jet velocities with the same jet diameter of 5.5mm. It is illustrated that there is nearly no damage observed on the surface and only a small amount of signal attenuation in C-scan result of a CFRP plate subjected to a 343m/s waterjet impact. When the velocity increases to 428m/s, a typical ring damage mainly caused by the resin removal appears on the surface, and the internal delamination area is also enlarged. If the velocity reaches 557m/s, the surface damage becomes more serious with the width and diameter of the failure ring increasing. Within the surface failure ring, not only the range of the resin removal expands, but also the matrix cracking appears along the fiber direction. The delamination damage area further increases, and presents a diamond-like shape. Results show that waterjet velocity is a crucial factor on the CFRP damage. With the jet velocity increasing, both the water-hammer pressure (Eq. (3)) and the stagnation pressure (Eq. (8)) are increased, and the specimen has to deform more and thus suffer more damage in order to absorb the increased impact energy.

The test and simulation results of the CFRP specimens under impacts of waterjets with the same velocity of 557m/s and different diameters are shown in Fig. 12. With the growth of the jet diameter, the surface annular damage continuously extends outward, with a wider area of resin removal and the occurrence of the matrix cracking along the fiber direction. When the jet diameter increases to 6.2mm, the faded "failure ring" is observed to be more apparent and the cracks become wider and deeper. The internal delamination damage always presents a typical diamond shape, and its projected region expands with jet diameter increasing. Results show that the damage patterns and their measuring parameters are basically well-predicted by the simulation, and waterjet

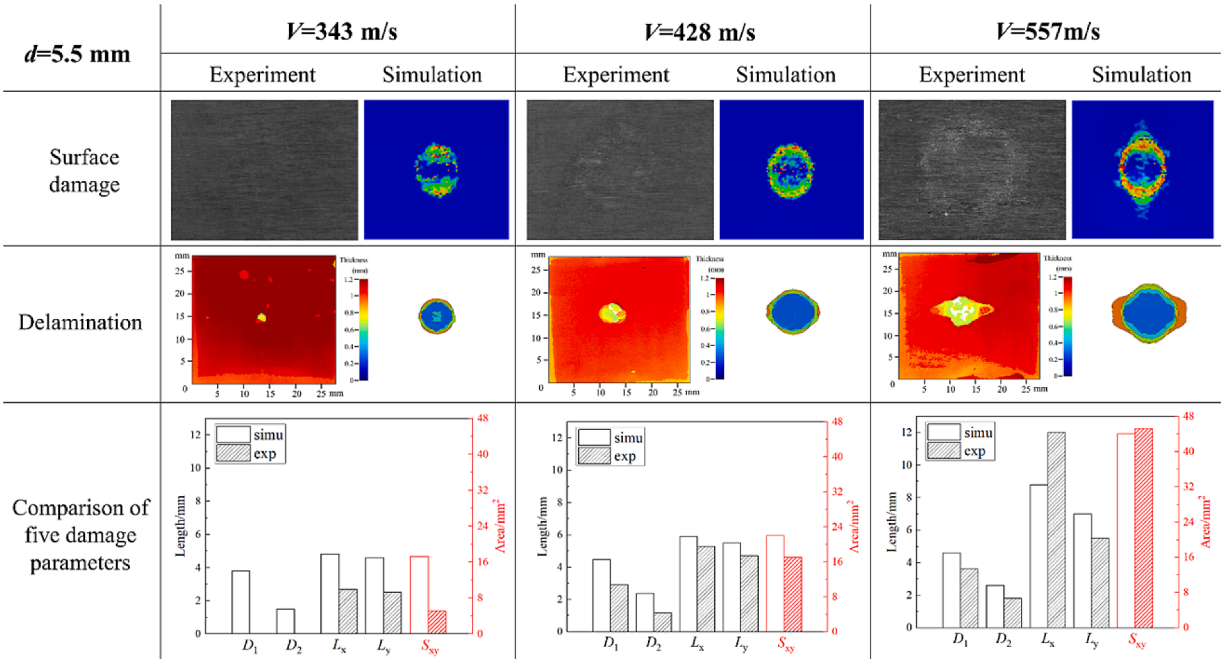

Fig 11. Simulation and experiment results of different jet velocities with the same jet diameter of 5.5mm.

diameter is also proved to have great influence on the CFRP damage. The larger the jet diameter is, the more the liquid mass will be and thus the higher impact energy is generated to cause more serious damage. In the perspective of the impact momentum, both the water-hammer pressure (Eq. (3)) and the stagnation pressure (Eq. (8)) have no relation with the waterjet diameter while the impulse duration (Eq. (6)) is dominated by the jet diameter. Therefore, the phenomenon that the damage increases with the waterjet diameter increasing can be attributed to the increased impulse duration.

Fig. 13 shows the quantitative variation of the internal damage area S_{xy} with the waterjet velocity increasing at three diameters by comparing the experiment and simulation results. It is further proved that the established numerical model can well predict the internal damage area of CFRP impacted by waterjets for higher speeds (over 400m/s). For relatively lower speeds (below 400m/s), the damage areas are overestimated due to the assumption in simulation that the waterjet profiles do not change with the velocity increasing, which is not the case in tests. Both the velocity and the diameter of the waterjet exert significant influences on the CFRP impact damage, since increasing the two factors directly results in the growth of the impact energy and the impulse of water-hammer pressure. There is a threshold of the jet velocity below which a single impact of a waterjet cannot result in any damage on the specified material. This parameter "single-shot threshold (SST)" was previously introduced in [22] and it is known to be decrease with the jet diameter increasing. According to experiment results in Fig. 13, the SST of the CFRP laminate in this study is about 300m/s for jets with the diameter of 5.5mm and 340m/s for 4.8mm jets.

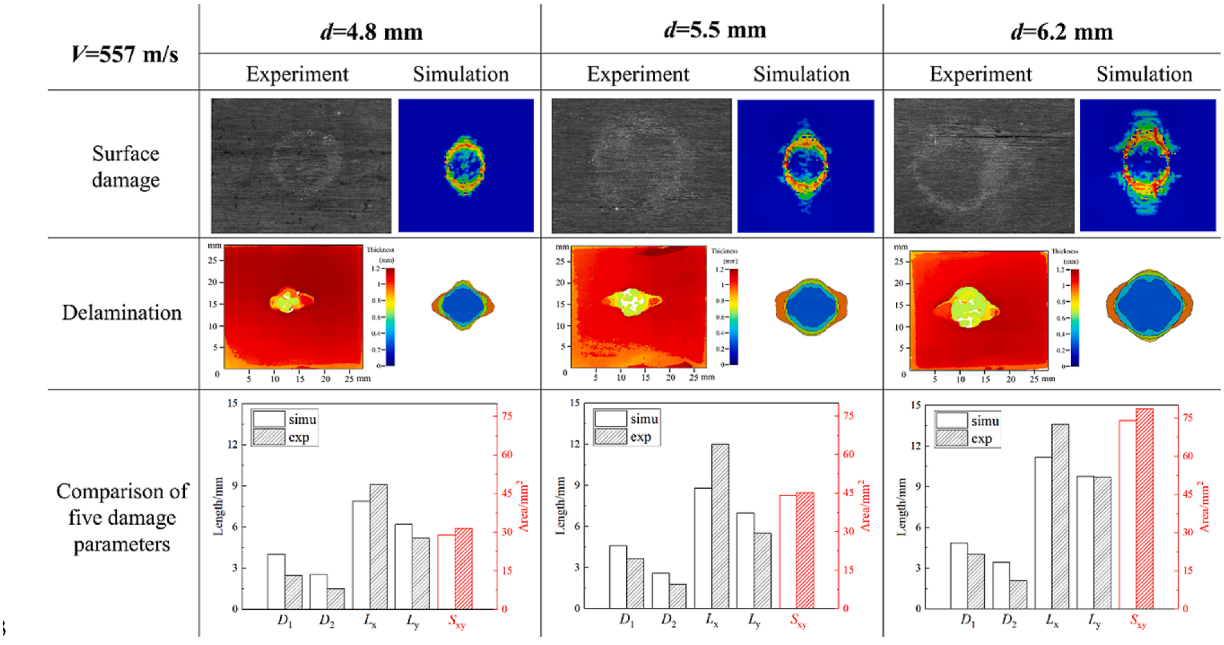

Fig 12. Simulation and experiment results of different jet diameters with the same jet velocity of 557m/s.

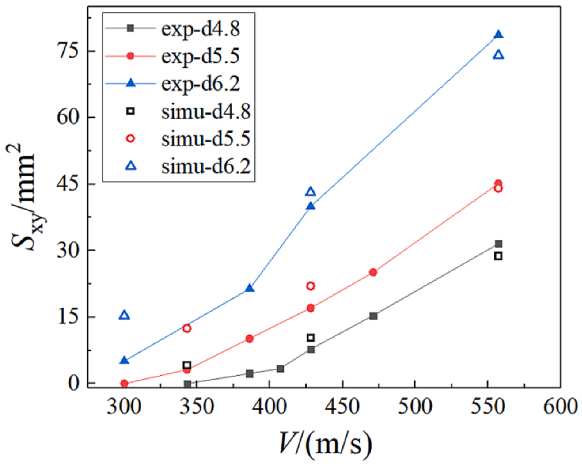

Fig 13. Simulation and experiment results of the internal damage area S_{xy} with respect to the waterjet velocity at three jet diameters.

5.4. Discussions on damage mechanism

The typical damage characteristics of the cross-ply CFRP laminate subjected to single waterjet impact are concluded and the mechanism of each damage mode is analyzed based on all the experiment and simulation evidence in the previous sections.

The typical damage on the surface presents a "failure ring" with a central region with no visible surface damage surrounded by resin removal, matrix cracking, and minor fiber fracture. According to the simulation results, matrix cracking is a kind of matrix tension damage which initiates at the ending moment of the water-hammer pressure and expands its scope due to the propagation of stress waves during the lateral jetting. Remarkably, the stagnation pressure used to be thought as little effect on the material damage because it is far lower than the strength of most studied isotropic materials [38]. In the present study, however, the stagnation pressure under high-speed impact (45MPa for 300m/s and 155MPa for 557m/s) exceeds the matrix tensile strength of the CFRP (Y_t=42MPa in Table 1) and thus cannot be ignored in composite damage analysis. Therefore, matrix cracking on the surface is caused by the release wave at the boundary of the contact radius and the stagnation pressure of lateral flow. Furthermore, resin removal and fiber exposure are believed to be the consequence of the shear stress exerted by the high-speed radial flow. According to previous investigations [11, 39], the lateral flow mainly corrodes the initial surface defects near the impact zone, and thus the smooth surface is relatively unaffected. This mechanism cannot be proved in the present simulation model since macro-mechanic homogenous strength theories are applied, which neglect the surface roughness and the difference of mechanical behaviors between the fiber and the matrix. Extra tests and micro-mechanical models will be implemented to verify it in the future.

The impacted surface is depressed near the impact location and the main incentive is the water-hammer pressure due to the following two reasons. One is the value of the water-hammer pressure (around 1GPa for 557m/s) is far higher than the transverse compression strength of the CFRP laminate in this study (Y_c=143MPa in Table 1). Although the duration of the water hammer pressure is only about 1 μs, it is sufficient to cause permanent deformation on solids [6,39]. Another evidence is the dimension of the crater is in accordance with that of the matrix compression failure in simulation, and the onset and evolution of the matrix compression damage agree well with the duration of the water-hammer pressure.

There is a string of matrix cracks along longitudinal direction observed at the back surface and the simulation results have shown that the onset of these cracks is related to the reflection of the compression wave. Additionally, the back cracks are constantly aggravated due to the propagation of stress waves within the specimen.

The projected area of the internal delamination damage presents a typical diamond-like shape with unequal dimensions when the impact velocity is over 500m/s. It is illustrated in simulation results that shear fracture (related to σ_{13} and σ_{23}) is the dominant failure mode in most delamination regions of all interfaces while only a minor delamination region near the impact center is dominated by normal fracture (related to σ_{33}). This points to the fact that most delamination area is caused by the bending shear stress generated in the impact event and minor delamination is due to the reflection of the compression wave at the back surface. Moreover, the load-bearing capacity along the longitudinal direction is higher than the transverse direction, so the average stress level is higher and the interface damage extents further, leading to unequal lengths of delamination.

It is observed in tests that the matrix cracking extends its scope from top to bottom at the cross-section view, which shows similar trend with the simulation results of the intralaminar matrix tensile damage. Therefore, the intralaminar matrix cracking is related to matrix tensile damage, initiating at the bottom layer due to the reflection of the compression wave, and propagates to the upper layers with the release tension wave.

6. Conclusions

In this paper, experiments of waterjets impacting on a cross-ply CFRP laminate were performed on a typical single waterjet generating apparatus and a finite element model of the CFRP-waterjet impingement event was established. The dynamic response and typical impact damage behavior of the CFRP laminate with high-speed waterjets (300~560m/s) were observed and the failure mechanisms were analyzed. Some highlights can be drawn as follows.

(1) The best estimation of the water-hammer pressure is given by Engel's equation as the compressibility of both the liquid and the solid is considered. The distribution of the water-hammer pressure is non-uniform within the contact region and the maximum pressure appears near the contact boundary when the shock wave is about to overtake. Mises stress generated on the surface along the longitudinal direction is larger than that along the transverse direction while such feature is not obvious in contact pressure.

(2) After a high-speed waterjet strikes a CFRP laminate, the impacted surface is depressed, and a central region with no visible surface damage is presented, surrounded by a faded "failure ring" in which there are resin removal, matrix cracking and minor fiber fracture. Delamination occurs at the interfaces of adjacent layers with unequal dimensions and longitudinal matrix cracks appear on the back surface. Both the velocity and diameter of the waterjets have significant effects on the damage of CFRP laminates.

(3) Matrix cracking on the top surface results from the release wave at the contact boundary and the stagnation pressure of lateral flow which is sufficiently larger than the CFRP transverse tensile strength. The surface pit is caused by matrix compression related to the water-hammer pressure. Reflection and propagation of stress waves within the specimen lead to interlaminar delamination, intralaminar matrix damage and the matrix cracking on the back surface.

Declaration of Competing Interest

We declare that we have no financial and personal relationships with other people or organizations that can inappropriately influence our work. There is no professional or other personal interest of any nature or kind in any product, service and/or company that could be construed as influencing the position presented in, or the review of, the manuscript entitled.

Acknowledgement

This work was supported by National Natural Science Foundation of China (Grant Number 11832015 and 12072289).

References

[1] Brunton JH, Field JE, Thomas GP. Deformation of solids by the impact of liquids, and its relation to rain damage in aircraft and missiles, to blade erosion in steam turbines, and to cavitation erosion. Nature 1965;207:925–6.
[2] Adler WF. Rain impact retrospective and vision for the future. Wear 1999;233:25–38.
[3] Field JE. ELSI conference: invited lecture - Liquid impact: theory, experiment, applications. Wear 1999;233:1–12.
[4] Gohardani O. Impact of erosion testing aspects on current and future flight conditions. Prog Aerosp Sci 2011;47:280–303.
[5] Bowden FPFRSB, J H. The deformation of solids by liquid impact at supersonic speeds. Proc R Society London. Series A. Math Phys Sci 1961;263:433–50.
[6] Bowden FPFRSF, J E. The brittle fracture of solids by liquid impact by solid impact and by shock. Proc R Soc Lond A 1964;282:331–52.
[7] Field JEG, D A, Hagan JT, Matthewson MJ, Swain Michael, Zwaag S. liquid jet impact and damge assessment for birttle solid. In: Proc. 5th Int. Conf. on Erosion by Solid and Liquid Impact, Cambridge; 1979. 13/11-13/11.
[8] Lu Y, Huang F, Liu X, Ao X. On the failure pattern of sandstone impacted by high-velocity water jet. Int J Impact Eng 2015;76:67–74.
[9] Momber AW. The response of geo-materials to high-speed liquid drop impact. Int J Impact Eng 2016;89:83–101.
[10] Hancox NL. The erosion of carbon fibre reinforced plastic by repeated liquid impact. Wear 1973;23:71–81.
[11] Gorham DAF, J E. The failure of composite materials under high-velocity liquid impact. J Appl Phys 1976;9:1529–41.
[12] Haller KK, Ventikos Y, Poulikakos D, Monkewitz P. Computational study of high-speed liquid droplet impact. J Appl Phys 2002;92:2821–8.
[13] Li R, Ninokata H, Mori M. A numerical study of impact force caused by liquid droplet impingement onto a rigid wall. Prog Nucl Energy 2011;53:881–5.
[14] Fujisawa K, Ohki M, Fujisawa N. Influence of surface roughness on liquid droplet impingement erosion. Wear 2019:432–3.
[15] Adler WF. Waterdrop Impact Modeling. Wear 1995;186:341–51.
[16] Bourne NK. On impacting liquid jets and drops onto polymethylmethacrylate targets. Proc R Soc A 2005;461:1129–45.
[17] C.-Y. Hsu, C.-C. Liang, T.-L. Teng, A.-T. Nguyen, A numerical study on high-speed water jet impact, Ocean Engineering, 72 (2013) 98-106.
[18] Cook S. Erosion by water-hammer. Proc R Soc London, Ser A 1928;119:481–8.
[19] Heymann FJ. On the shock wave velocity and impact pressure in high speed liquid-solid impact, transactions of the ASME, series D. J Basic Eng 1968;90:400–2.
[20] Engel OG. Damage produced by high-speed liquid-drop impacts. J Appl Phys 1973;44:692–704.
[21] Springer GS, Yang CI. Model for the Rain Erosion of Fiber Reinforced Composites. AIAA J 1975;13:877–83.
[22] Kennedy CF, Field JE. Damage threshold velocities for liquid impact. J Mater Sci 2000;35:5331–9.
[23] Field JE. The physics of liquid impact, shock wave interactions with cavities, and the implications to shock wave lithotripsy. Phys Med Biol 1991;36:1475–84.
[24] Obara T, Bourne NK, Field JE. Liquid-Jet Impact on Liquid and Solid-Surfaces. Wear 1995;186:388–94.
[25] Klocek P, Seward CR, Pickles CSJ, Field JE. Single and multiple impact jet apparatus and results. Window and dome technologies and materials II. San Diego: SPIE; 1990. p. 280–90.
[26] Burson-Thomas CB, Wellman R, Harvey TJ, Wood RJK. Water droplet erosion of aeroengine fan blades: The importance of form. Wear 2019;426-427:507–17.
[27] Kirols HS, Kevorkov D, Uihlein A, Medraj M. The effect of initial surface roughness on water droplet erosion behaviour. Wear 2015;342-343:198–209.
[28] Fujisawa N, Takano S, Fujisawa K, Yamagata T. Experiments on liquid droplet impingement erosion on a rough surface. Wear 2018;398-399:158–64.
[29] Tan W, Falzon BG, Chiu LNS, Price M. Predicting low velocity impact damage and Compression-After-Impact (CAI) behaviour of composite laminates. Composites, Part A 2015;71:212–26.
[30] Li X, Ma D, Liu H, Tan W, Gong X, Zhang C, Li Y. Assessment of failure criteria and damage evolution methods for composite laminates under low-velocity impact. Compos Struct 2019;207:727–39.
[31] Gingold RA, Monaghan JJ. Smoothed particle hydrodynamics - theory and application to non-spherical stars. Mon Not R Astron Soc 1977;181:375–89.
[32] Hou JPP, N, Ruiz C, Hallett SR. Prediction of impact damage in composite plates. Comp Sci Technol 2000;60:273–81.
[33] Lapczyk I, Hurtado JA. Progressive damage modeling in fiber-reinforced materials. Composites, Part A 2007;38:2333–41.
[34] Camanho PP, Davila CG, de Moura MF. Numerical simulation of mixed-mode progressive delamination in composite materials. J Compos Mater 2016;37:1415–38.
[35] Benzeggagh ML, Kenane M. Measurement of mixed-mode delamination fracture toughness of unidirectional glass/epoxy composites with mixed-mode bending apparatus. Compos Sci Technol 1996;56:439–49.
[36] Hamashima H. Determination of JWL parameters for non-ideal explosive. In: AIP Conference Proceedings; 2004. p. 331–4.
[37] Lou X, Cai H, Yu P, Jiao F, Han X. Failure analysis of composite laminate under low-velocity impact based on micromechanics of failure. Compos Struct 2017;163:238–47.
[38] Bourne NK, Obara T, Field JE. High-speed photography and stress gauge studies of jet impact upon surfaces. Philos T R Soc A 1997;355:607–23.
[39] Brunton JH. The physics of impact and deformation single impact High speed liquid impact. Philos T R Soc A 1966;260:79–85.